Asynchronous current-induced switching of rare-earth and transition-metal sublattices in ferrimagnetic alloys

Giacomo Sala[1]*, Charles-Henri Lambert[1], Simone Finizio[2], Victor Raposo[3], Viola Krizakova[1], Gunasheel Krishnaswamy[1], Markus Weigand[4], Jorg Raabe[2], Marta D. Rossell[5], Eduardo Martinez[3], and Pietro Gambardella[1]*

[1]Department of Materials, ETH Zurich, 8093 Zurich, Switzerland.
[2]Swiss Light Source, Paul Scherrer Institut, 5232 Villigen PSI, Switzerland.
[3]Departamento de Física Aplicada, University of Salamanca, 37008 Salamanca, Spain.
[4]Max Planck Institute for Intelligent Systems, 70569 Stuttgart, Germany.
[5]Electron Microscopy Center, Empa, Swiss Federal Laboratories for Materials Science and Technology, 8600 Dübendorf, Switzerland
*Email: giacomo.sala@mat.ethz.ch (G.S.); pietro.gambardella@mat.ethz.ch (P.G.)

1 **Abstract**

2 Ferrimagnetic alloys are model systems for understanding the ultrafast magnetization switching
3 in materials with antiferromagnetically-coupled sublattices. Here we investigate the dynamics of
4 the rare-earth and transition-metal sublattices in ferrimagnetic GdFeCo and TbCo dots excited
5 by spin-orbit torques with combined temporal, spatial, and elemental resolution. We observe
6 distinct switching regimes in which the magnetizations of the two sublattices either remain syn-
7 chronized throughout the reversal process or switch following different trajectories in time and
8 space. In the latter case, we observe a transient ferromagnetic state that lasts up to 2 ns. The
9 asynchronous switching of the two magnetizations is ascribed to the master-agent dynamics in-
10 duced by the spin-orbit torques in combination with the weak antiferromagnetic coupling, which
11 depends sensitively on the microstructure of ferrimagnets. A larger antiferromagnetic exchange
12 between the two sublattices leads to faster switching and shorter recovery of the magnetization
13 after a current pulse.

1

Ferrimagnetic alloys have raised strong interest owing to their ultrafast magneto-optical switching properties [1–5] and high speed current-induced magnetic domain wall motion [6–8]. These characteristics make ferrimagnets optimal candidates for nonvolatile memory applications [5, 9–11] as well as for testing models of magnetization dynamics in multi-element systems [7, 12–19]. Several rare-earth (RE) transition-metal (TM) alloys are ferrimagnetic because the localized $4f$ magnetic moments of the RE and the itinerant $3d$ moments of the TM couple antiparallel to each other, forming two spin sublattices with distinct properties that can be tuned by composition and temperature [20]. In particular, the total magnetization and angular momentum vanish at the respective compensation points, which makes the magnetization dynamics immune to external fields and extremely fast.

This dynamics can be quite surprising. Intense laser pulses as short as 40 fs can toggle the magnetization of RE-TM ferrimagnets without assisting magnetic fields [1, 3, 5]. This all-optical switching involves an unusual transient ferromagnetic state [21, 22] during which the RE and TM magnetizations attain the same orientation for a few ps. The ferromagnetic alignment results from the interplay of ultrafast heating and the transfer of angular momentum between two spin sublattices with distinct demagnetization rates, and is instrumental in achieving fast switching [16, 18, 23, 24]. Besides optical means, the magnetic order of RE-TM ferrimagnets can be manipulated by current-induced heat [25, 26] and spin-orbit torques (SOT) [27]. Whereas intense ps-long heat pulses have a toggling effect similar to all-optical switching [25, 26], SOT induce bipolar switching [28–32] and directional domain wall motion with velocities of up to 5 km/s close to the angular momentum compensation point [6–8]. In general, however, the response of the RE and TM spin sublattices to an electric current can be more complex than considered so far, both in the temporal and spatial domain. In contrast to all-optical switching, for which the role of the RE and TM sublattices has been intensively investigated [15, 18, 21, 22], the RE and TM magnetic moments are considered to be steadily coupled to each other during current-induced switching and domain wall motion, similar to antiferromagnets [33, 34]. Testing this assumption is important to understand the SOT-induced dynamics of ferrimagnets as well as to optimize their magnetization reversal speed.

Here, we present a study of the SOT-induced magnetization switching of RE-TM ferrimagnets that combines time-, space-, and element-resolution. By using scanning transmission X-ray microscopy (STXM) and X-ray magnetic circular dichroism (XMCD), we probe the evolution of the RE and TM magnetizations excited by sub-ns and ns-long current pulses. While being antiferromagnetically coupled in equilibrium, the two sublattices can evolve asynchronously in time and inhomogeneously in space during and after the electric pulses. This difference takes the form of a delay between domain walls in the two sublattices or, in the extreme case, of a transient ferromagnetic state that can last as long as 2 ns. Our measurements, combined with
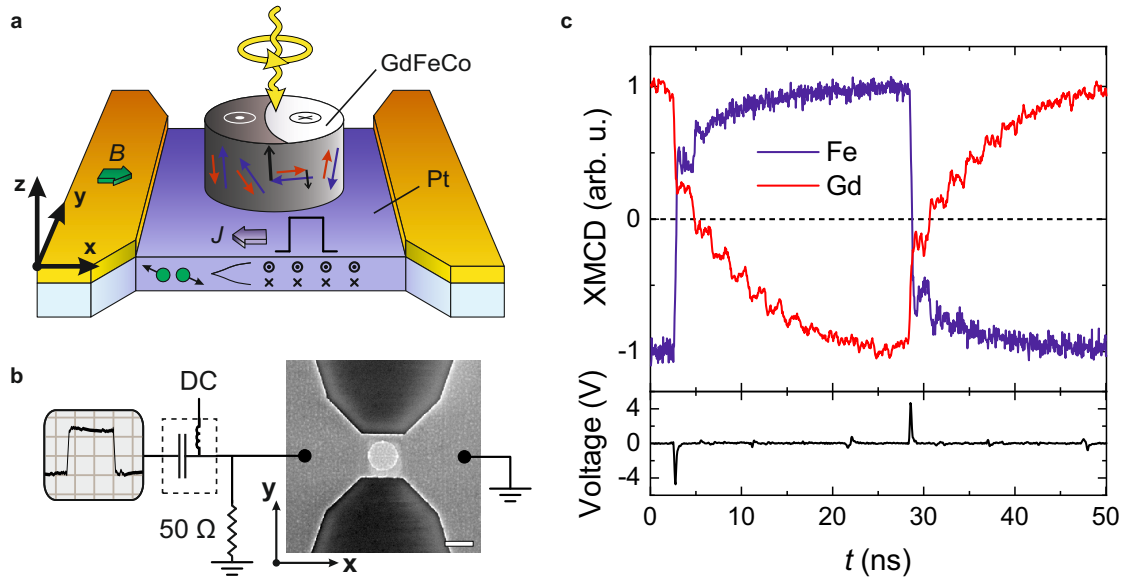
2

Fig. 1 | Time-, space-, and element-resolved current-induced switching of GdFeCo. a, Schematic of the sample layout, which consists of a ferrimagnetic GdFeCo dot on top of a Pt current line. The current pulse J induces the switching of the RE and TM magnetizations by SOT. **b,** Scanning electron micrograph of the device and schematic of the electric setup used for its excitation. The scale bar corresponds to 1 μm. **c,** Time-dependence of the spatially-averaged XMCD signal at the Fe L_3 and Gd M_5 edges measured while applying bipolar electric pulses with 200 ps duration (FWHM) and 4.8 V amplitude ($J \sim 1.3 \cdot 10^{12}$ A/m^2) to a Gd$_{31}$Fe$_{62}$Co$_7$ dot. A static magnetic field $B = 25$ mT was applied parallel to the current direction to define the switching polarity. The bottom panel shows the amplitude and duration of the voltage pulses.

1 micromagnetic simulations, reveal that the speed of the magnetization reversal in RE-TM ferri-
2 magnets depends critically on the antiferromagnetic exchange coupling between the RE and TM
3 sublattices, which is determined by the microstructure of the RE-TM alloy.

Magnetization reversal of the TM and RE sublattices

5 We employed a stroboscopic current-pump, X-ray-probe imaging technique to study amorphous
6 ferrimagnetic alloys of GdFeCo(15 nm) and TbCo(4 nm) with perpendicular anisotropy, shaped
7 into circular dots with diameter of 0.5 or 1 μm (see Methods and Supplementary Notes 1-2). The
8 dots were fabricated on top of a Pt(5 nm) layer that served for the injection of electric pulses,
9 as shown in Fig. 1a,b. The devices were excited with a repeated sequence of set-reset pulses
10 with alternating polarity that toggled the magnetization via the SOT [27, 35]. The dynamics of
11 the z magnetization component of each sublattice was detected by measuring the transmission
12 through the sample of circularly polarized X-rays tuned to the L_3 and M_5 absorption edges of
13 the TM and RE elements, respectively. The X-ray beam, which consisted of 70-ps-long X-ray
14 pulses synchronized to the current excitation, was raster-scanned over the sample with a spatial

3

resolution of 35 nm (see Methods).

The XMCD traces in Fig. 1c represent the time dependence of the spatially-averaged magnetic contrast measured at the Fe and Gd edges in a $Gd_{31}Fe_{62}Co_7$ dot excited by 200-ps long electric pulses. The switching a 1-μm-wide dot by 200-ps pulses confirms the fast current-induced dynamics of ferrimagnets. At equilibrium, Fe and Gd have opposite XMCD contrast, as expected from the antiparallel orientation of their magnetizations, $\mathbf{M}_{Fe}$ and $\mathbf{M}_{Gd}$. At each electric pulse, both $\mathbf{M}_{Fe}$ and $\mathbf{M}_{Gd}$ switch to the opposite state. Their final up or down orientation is determined by the polarity of the pulse and the direction of the magnetic field applied collinear to the current, as typical of SOT [27, 35]. However, the reversal path followed by Fe and Gd is unexpected and very different from the switching trajectory observed in ferromagnets. First, rather than switching during the electric pulse [36], the process involves two phases: an abrupt transition and a slow oscillatory evolution towards equilibrium that is particularly pronounced in Gd. Second, although both sublattices share this two-phase dynamics, they switch asynchronously with respect to each other, as indicated by the different times at which the traces cross zero. Whereas $\mathbf{M}_{Fe}$ reverses its direction during the electric pulse, $\mathbf{M}_{Gd}$ maintains its original orientation. Only 2 ns after the pulse onset does $\mathbf{M}_{Gd}$ switch. Thus, the two magnetizations attain an average transient ferromagnetic state on the ns timescale.

Spatially resolved dynamics

To better visualize the reversal process, we increased the pulse length to 1 ns, as shown in Fig. 2a. Similarly to the switching with 200-ps pulses, the reversal proceeds via a rapid transition and a slow oscillatory phase, with a temporary ferromagnetic alignment of the two sublattices that persists well beyond the end of the electrical excitation. The underlying switching process is clarified by the frames in Fig. 2b, which display snapshots of the magnetization in the two sublattices. The reversal of $\mathbf{M}_{Fe}$ involves the nucleation of a domain at the edge of the dot and the motion of a domain wall across the device with a speed of 0.8-1.3 km/s depending on the applied current density. We attribute this behavior to the interplay of SOT, Dzyaloshinskii-Moriya interaction, and magnetic field, in analogy to ferromagnetic systems [36, 37].

The dynamics of the Gd sublattice is substantially slower than that of Fe. No clear domain wall appears in Gd during the pulse. Instead, the magnetic contrast diminishes starting from the edges, but only partially, so that $\mathbf{M}_{Fe}$ and $\mathbf{M}_{Gd}$ attain the same orientation at the end of the pulse, as exemplified in the sketch. Only 1 ns after the pulse, a domain appears to expand in the Gd sublattice from the left to the right side, thus reestablishing the antiferromagnetic alignment between Gd and Fe. After about 3 ns from the onset of the pulse, no additional changes are observed in the two sublattices apart from a progressive increase of the magnetic contrast (see Supplementary Movie 1). This intensification corresponds to the slow after-pulse dynamics evidenced by Figs. 1c and 2a, which is also accompanied by temporal oscillations of the magnetic
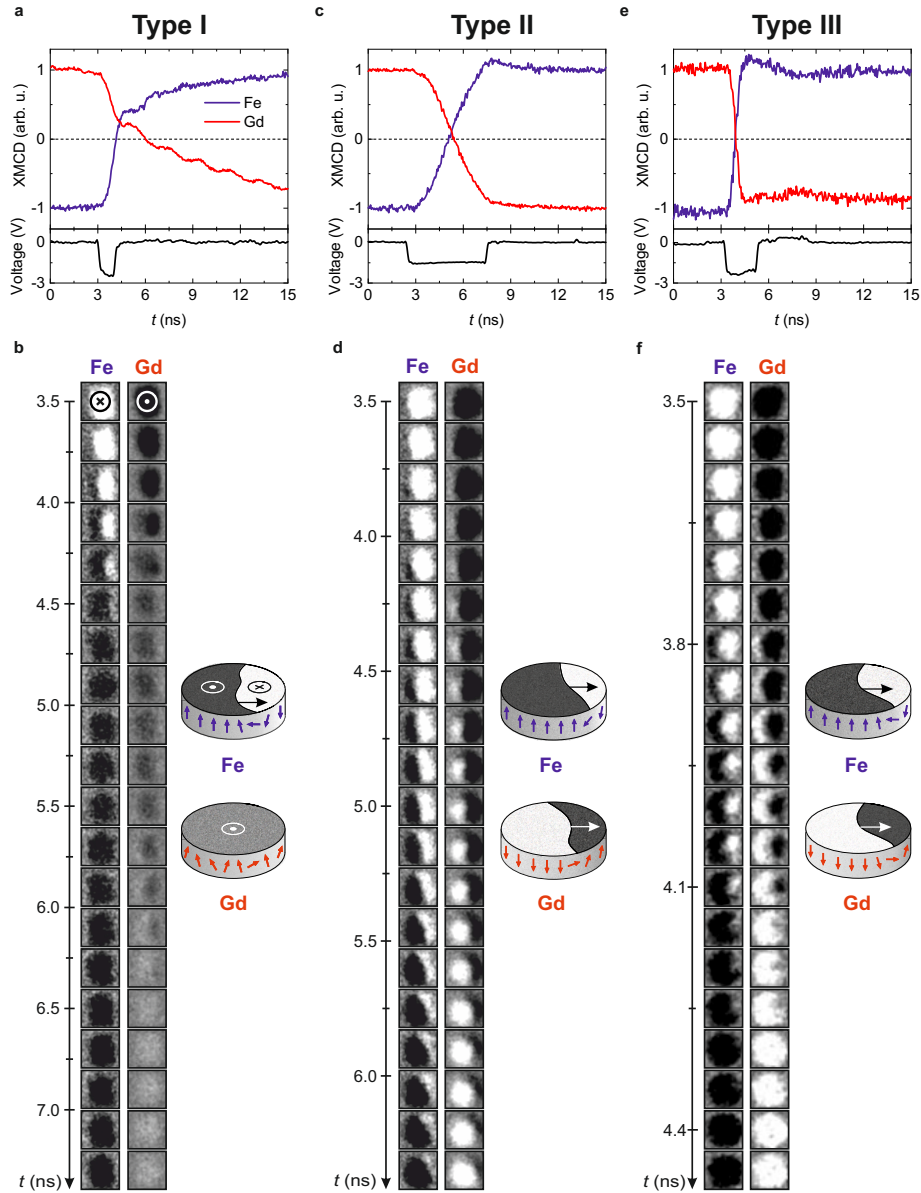
4

Fig. 2 | Switching dynamics of GdFeCo. a, c, e, Time dependence of the spatially-averaged XMCD contrast at the Fe and Gd edges for three distinct devices. The device composition is $Gd_{31}Fe_{62}Co_7$, $Gd_{30}Fe_{63}Co_7$, and $Gd_{29}Fe_{64}Co_7$ in **a,c,e**, respectively. The electric pulses, plotted in the bottom panels, have a duration of 1 ns, 5 ns, and 2 ns, and amplitude of -2.5 V, -1.4 V, and -2.3 V, respectively. A voltage of 2.5 V corresponds to an approximate current density of $\sim 0.7 \cdot 10^{12}$ A/m^2. The in-plane magnetic field was 20 mT, 10 mT, and 20 mT, respectively. **b, d, f**, Snapshots of the dynamics in **a**, **c**, **e**, respectively, and corresponding schematics. The vertical axis defines the timing of the frames. The dynamics in **a, b** was measured in the same device shown in Fig. 1c.
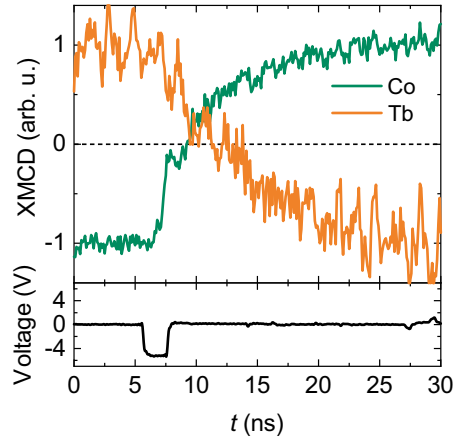
5

Fig. 3 | Switching dynamics of TbCo. Time dependence of the spatially-averaged XMCD contrast at the Co and Tb edges of a 500-nm-wide $Tb_{19}Co_{81}$ dot excited by 2-ns-long electric pulses with 5.1 V amplitude. The in-plane magnetic field was 110 mT.

1 contrast. Micromagnetic simulations identify the origin of the slow dynamics and its oscillations
2 with the combination of delayed domain nucleation events and collective magnetization preces-
3 sion, as discussed later. Our measurements show that this behavior is observed for both down-up
4 and up-down switching upon reversing the polarity of the current, is independent of the pulse
5 length/amplitude and strength of the in-plane magnetic field, and is not caused by Joule heating.
6 Finally, we do not identify differences between the magnetization of Fe and Co, which remain
7 ferromagnetically coupled (see Supplementary Notes 3-5).

8   Beside this dynamics, which we label type I, we found two additional switching regimes in
9 devices that differ by their microstructure and composition. These regimes, unlike the type I,
10 involve a single phase that terminates before the end of the pulse without further slow changes
11 of the magnetization. In addition, domain walls move in both sublattices. The type II dynamics,
12 shown in Fig. 2c,d, is characterized by the asynchronous motion of the Fe and Gd domain walls,
13 which are decoupled: in time, with a small but measurable delay of about 200 ps, and in space,
14 with different profiles across the dot (see also Supplementary Note 3 and Supplementary Movie
15 2).

16   Last, $\mathbf{M}_{Fe}$ and $\mathbf{M}_{Gd}$ can also switch by preserving antiparallel coupling throughout the whole
17 process. In this type III dynamics, the edge nucleation of a domain occurs at the same time in
18 Fe and Gd, and the domain walls propagate together without a measurable delay (see Supple-
19 mentary Movie 3). The type III corresponds to the scenario normally assumed in the modeling
20 of current-induced switching and domain wall motion in ferrimagnets, namely, the rigid antifer-
21 romagnetic coupling between the two sublattices.

22   This unexpected dynamics is not limited to GdFeCo. Also $Tb_xCo_{1-x}(4)$ alloys and $[Tb(0.25)/Co(0.25)]_6$
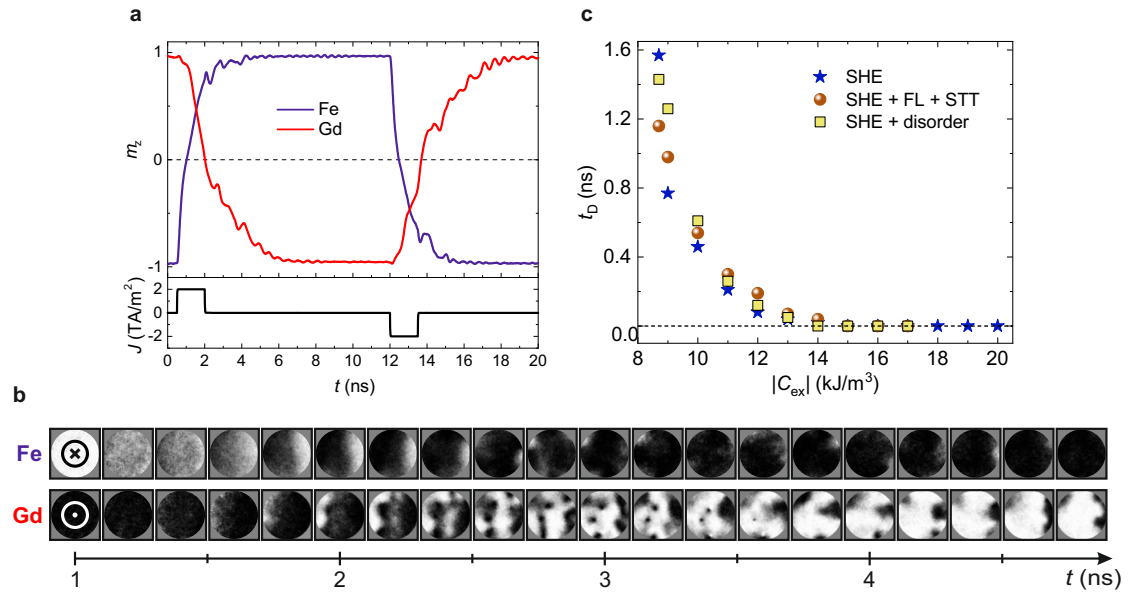
6

Fig. 4 | Micromagnetic simulations of the asynchronous dynamics. **a**, Time dependence of the simulated average component m_z of $\mathbf{M}_{Fe}$ and $\mathbf{M}_{Gd}$ excited by an electric pulse with 1.5 ns duration and a current density of 2 TA/m^2 when C_{ex} = -6.8 kJ/m^3. **b**, Snapshots of the magnetization switching induced by the first electric pulse in **a**. **c**, Delay $t_d = t_{Fe} - t_{Gd}$ between the times at which the m_z components of $\mathbf{M}_{Fe}$ and $\mathbf{M}_{Gd}$ cross zero as a function of the antiferromagnetic exchange energy density $|C_{ex}|$. The simulations assume $\theta_{SH}^{TM} = 0.21$, $\theta_{SH}^{RE} = 0.07$ and damping-like SOT (stars), field-like torque and spin transfer torque (circles), thermal fluctuations and grains of 10 nm size with 10% random variations of the magnetic anisotropy (squares), see Methods.

multilayers present asynchronous switching regimes (see Supplementary Note 6). For example, Fig. 3 shows the temporal evolution of the spatially-averaged XMCD contrast measured at the Tb and Co edges in a $Tb_{19}Co_{81}$ dot excited by 2-ns-long current pulses. The small thickness of TbCo limits the signal quality and hinders the detection of the spatial details of the dynamics. However, the traces present the same features as the dynamics of type I of GdFeCo, namely, the faster switching of the TM sublattice and a ferromagnetic state lasting for about 1 ns.

These measurements disclose the existence of multiple switching paths in RE-TM ferrimagnets characterized by a variable degree of coupling between the two sublattices. Extensive experiments confirm that this variability is an intrinsic property of each sample, independent of the amplitude and duration of the electric pulses, as well as of the applied magnetic field (Supplementary Note 4). Moreover, the type of dynamics is not simply associated with the sample stoichiometry because devices with equal composition show distinct reversal regimes (Supplementary Note 6).

Micromagnetic modelling

To rationalize such diversified dynamics, we performed micromagnetic simulations of the switch-

7

ing caused by SOT in RE-TM ferrimagnets, in which $\mathbf{M}_{Fe}$ and $\mathbf{M}_{Gd}$ are separately described by two coupled Landau-Lifschitz-Gilbert equations (see Methods and Ref. [38]). Since the major contribution to $\mathbf{M}_{Gd}$ comes from the localized $4f$ electrons, which lie about 4 eV below the Fermi level, the magneto-transport properties of RE-TM ferrimagnets depend mostly on the $3d$ electrons of the TM element [39–42]. Thus, the SOT are expected to interact predominantly with the TM magnetic moments and be transferred to the RE sublattice indirectly through the RE-TM exchange interaction. This imbalance was taken into account by adopting element-dependent effective spin Hall angles. In this scenario, our simulations reproduce the three types of dynamics under the assumption of a variable antiferromagnetic coupling, whose strength is modelled by the exchange energy per unit volume C_{ex} (see Methods and Supplementary Note 7). In the following, we consider GdFeCo as model system but similar considerations apply to TbCo.

Figure 4a,b shows the simulated dynamics of the Fe and Gd sublattices triggered by 1.5-ns-long pulses with $2 \cdot 10^{12}$ A/m² current density assuming effective spin Hall angles $\theta_{SH}^{TM} = 0.21$, $\theta_{SH}^{RE} = 0.07$, and C_{ex} = -6.8 kJ/m³. The simulations reproduce all the main features of the type I dynamics shown in Fig. 1c and Fig. 2a,b, namely, the switching by domain nucleation and propagation in Fe but not in Gd, the formation of the transient ferromagnetic state, and the after-pulse slow recovery of the magnetization. Upon injection of the pulse, the SOT trigger the switching of $\mathbf{M}_{Fe}$. For a sufficiently large current, this process is almost instantaneous [32]. However, since the effect of the SOT on $\mathbf{M}_{Gd}$ is small, the latter can switch only if dragged by the antiferromagnetic exchange torque [43]. This is a turbulent process without a reproducible spatial pattern because it develops when $\mathbf{M}_{Fe}$ has already completed the switching, which results in the weak homogeneous XMCD contrast observed in Fig. 2b. At the same time, the average perpendicular component of $\mathbf{M}_{Gd}$ oscillates around the total perpendicular field resulting from the exchange and anisotropy fields, in agreement with the oscillations visible in Fig. 1c and 2a.

The switching dynamics transitions from type I to type III in a narrow range of C_{ex} (see Fig. 4c and Supplementary Notes 8 and 9). For $| C_{ex} | \geq 11$ kJ/m³, the switching is mediated by the displacement of a domain wall in both the Fe and Gd sublattices. A finite delay exists between the two domain walls for intermediate values of C_{ex}, whereas for $| C_{ex} | \geq 14$ kJ/m³ the two magnetizations remain rigidly coupled during the entire process. Small variations of the saturation magnetization and magnetic anisotropy lead to better agreement of the simulations of different samples, but are not essential to reproduce the type of dynamics. Simulations performed for different values of the applied magnetic field, spin-transfer torque, field-like SOT, Dzyaloshinkii-Moriya interaction, or by including thermal fluctuations, defects, and random spatial variations of the magnetic parameters do not reproduce the transition between the three dynamic regimes. The precise value of θ_{SH}^{RE} is also not fundamental to reproduce the experimen-

1. tal dynamics provided that $\theta_{SH}^{RE} < \theta_{SH}^{TM}$. Thus, the sole parameter that allows us to replicate the
2. ns-long ferromagnetic state and the change of switching regime is C_{ex}.

3. We summarize these findings in Fig. 4c by simulating the delay time t_D of $\mathbf{M}_{Gd}$ with re-
4. spect to $\mathbf{M}_{Fe}$ as a function of C_{ex} (all of the other parameters are fixed). We find that t_D rapidly
5. diminishes as C_{ex} becomes larger, whose increase also results in a overall faster dynamics, as
6. expected for antiferromagnets (see Supplementary Note 10). The simulations clarify that the
7. asynchronous switching originates from the weak and variable antiferromagnetic coupling be-
8. tween the RE and TM sublattices in conjunction with the master-slave dynamics induced by
9. the SOT. While the latter is ascribed to the different localization of the electronic orbitals and
10. density of states at the Fermi level of the RE and TM elements [40–42], we find that the former
11. is linked to the composition and microstructure of the ferrimagnetic alloy, as discussed next.

Discussion

13. The asynchronous sublattice magnetization dynamics reported here is reminiscent of all-optical
14. switching observed in GdFeCo alloys [3, 5, 21, 22]. Yet, our measurements show that the
15. decoupling of the RE and TM magnetization dynamics is a general feature of RE-TM alloys
16. that extends well beyond the ultrafast temporal regime of all-optical switching and involves also
17. spin torque excitations. Moreover, in contrast with the toggling of the magnetization induced
18. by ultrafast heat pulses [25], the switching of GdFeCo and TbCo induced by SOT depends
19. on the polarity of the current and is not limited to ps-long pulses. Joule heating associated to
20. the current plays a role in activating domain nucleation [32], but the temperature increase in
21. our devices is too slow and moderate (< 8 K/ns, see Supplementary Note 5) to induce thermal
22. toggling of the magnetization [25]. Another specific feature of current-induced switching is the
23. coherent domain wall motion in the TM sublattice accompanied by either disordered or delayed
24. domain wall dynamics in the Gd sublattice in the type I or type II switching, respectively. Most
25. importantly, a transient ferromagnetic state is not a prerequisite for switching, as indeed observed
26. in the type III dynamics, because the reversal can directly occur due to the net transfer of angular
27. momentum from the electric current to the magnetization. Besides these phenomenological
28. considerations, all-optical and current-induced switching are fundamentally different because
29. ultrafast heating involves relaxation of the longitudinal magnetization, whereas the spin torque
30. dynamics is determined by the relaxation of the transverse component of the magnetization.
31. The relaxation rate is proportional to the RE-TM exchange coupling in the first case, and to the
32. effective magnetic field generated by the SOT in the second case [44]. Therefore, the observation
33. of a ns-long nonequilibrium ferromagnetic state cannot be explained by the thermal collapse of
34. the longitudinal magnetization of the TM sublattice, as in all-optical switching. Such a long-
35. lived transient state can only be rationalized by assuming uneven transfer of angular momentum
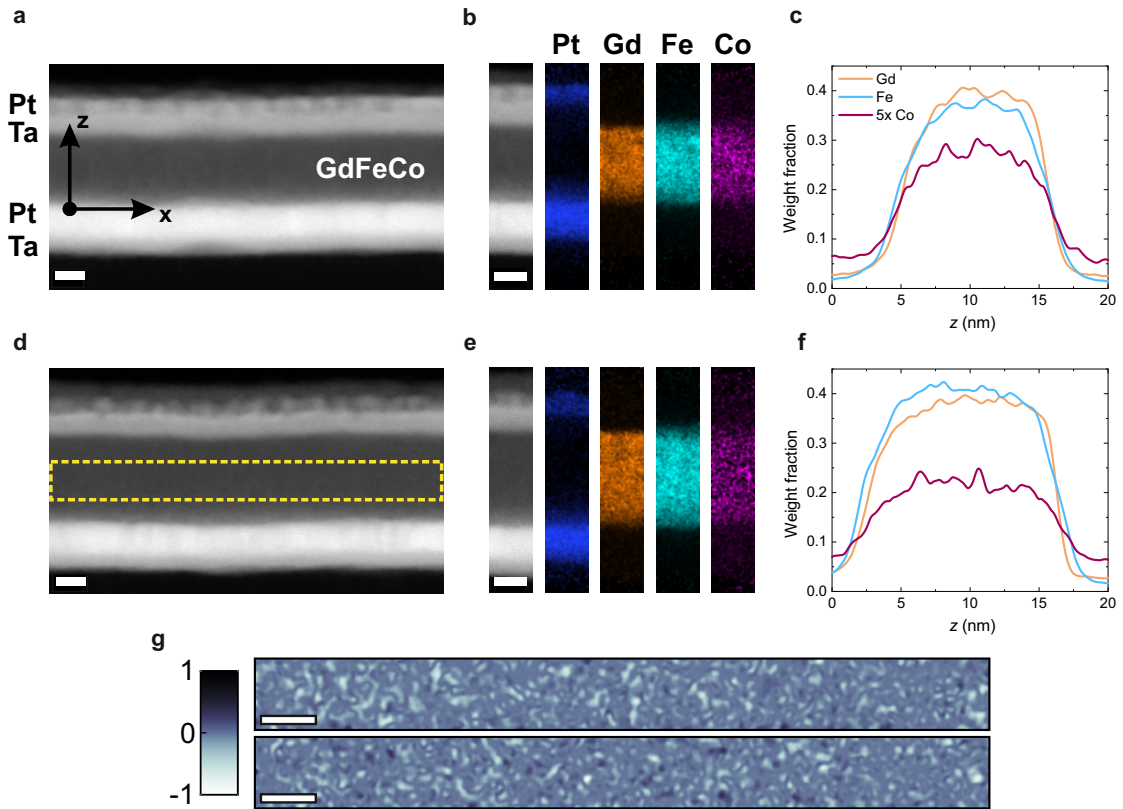36. from the electric current to the TM and RE sublattices and a relatively weak coupling among

9

Fig. 5 | Microstructure of fresh and aged GdFeCo films. **a**, STEM micrograph of a $Gd_{31}Fe_{62}Co_7$ blanket film characterized one month after growth. **b**, Magnified STEM image and STEM-EDX elemental maps of the constitutive elements. **c**, Profiles of the Fe and Gd concentration across the sample thickness. The profiles are averaged along the *x* direction in **a**. **d-f**, The same as **a-c** for a nominally-identical sample deposited simultaneously to the device in Figs. 1c, 2a,b and characterized 30 months after growth. **g**, Correlation image of the Fe and Gd concentration in the fresh (top) and aged (bottom) sample corresponding to the dashed rectangle in **d**. The correlation coefficients calculated from the two images are -0.50 and -0.40, respectively. The correlation coefficients obtained from the Fe and Gd line profiles are -0.65 and -0.37 in the fresh and aged samples, respectively, see Methods. The scale bars correspond to 5 nm.

them, in agreement with results of our micromagnetic simulations. The combination of these two factors is responsible for the master-agent dynamics between the TM and RE magnetization observed in type I and II switching.

Measurements performed in a period of one year in 20 devices differing in composition and age indicate a correlation between the time passed since the sample growth and the change of the dynamics from type I to type III as the samples aged (Supplementary Note 6). Although changes of stoichiometry can also play a role, this trend suggests that aging processes affect the antiferromagnetic coupling between the RE and TM sublattices most. To test this possibility,

10

we have characterized nominally identical "fresh" and "aged" GdFeCo samples using scanning transmission electron microscopy and energy-dispersive X-ray spectroscopy (STEM-EDX, see Methods). The structural and elemental maps in Fig. 5 show that GdFeCo has an amorphous structure with nanoscale inhomogeneous distributions of Fe, Co, and Gd. This inhomogeneity is present in both samples, but is more pronounced in the fresh sample, where the degree of anticorrelation between Fe and Gd is highest as estimated from the elemental concentration profiles (Fig. 5c,f) and autocorrelation maps (Fig. 5g) (see Supplementary Note 12). These results show that phase segregation takes place in RE-TM films, in agreement with previous studies [24, 45, 46]. The formation of Gd-rich and Fe-rich clusters prevents direct interactions between the TM and RE atoms [47], leading to a strong decrease of their antiferromagnetic coupling C_{ex} as compared to the homogeneous phase (see Supplementary Note 7). However, because the mixing enthalpy of TM and RE atoms is negative [48], the intermixing of the two species increases with time [49, 50], in agreement with our STEM observations. This structural relaxation affects C_{ex} and, ultimately, the type of dynamics during the SOT-induced switching.

In summary, our measurements reveal that the RE and TM sublattices of ferrimagnetic alloys can respond either synchronously or asynchronously to spin torques. We observe domain-wall speeds exceeding 1 km/s and switching with 200-ps-long current pulses in 1-μm-wide devices. This rapid dynamics is the fingerprint of ferrimagnets. However, the two magnetic sublattices are not rigidly coupled and respond differently to SOT, which leads to spatially and temporally inhomogeneous dynamics. We identified three switching regimes, characterized by domain nucleation and propagation in the TM sublattice and I) a transient ferromagnetic state followed by slow and spatially inhomogeneous reversal of the RE sublattice, II) delayed domain wall propagation in the RE sublattice, and III) synchronous switching of the RE sublattice. Micromagnetic simulations rationalize this behavior in terms of the antiferromagnetic exchange energy density, which varies in response to thermodynamically-driven relaxation processes that alter the atomic structure of the RE-TM alloy. Our results have practical implications for tuning the composition and microstructure of ferrimagnetic alloys utilized in spintronic devices to achieve maximum and uniform switching speed with minimal after-pulse dynamics. Moreover, they provide insight into the magnetization reversal of antiferromagnetically-coupled systems that is complementary to that obtained for all-optical switching at ultrafast timescales.

References

1. Stanciu, C. D. *et al.* All-Optical Magnetic Recording with Circularly Polarized Light. *Physical Review Letters* **99,** 047601 (2007).

2. Vahaplar, K. *et al.* Ultrafast Path for Optical Magnetization Reversal via a Strongly Nonequilibrium State. *Physical Review Letters* **103,** 66–69 (2009).

3. Kirilyuk, A. *et al.* Laser-induced magnetization dynamics and reversal in ferrimagnetic alloys. *Reports on Progress in Physics* **76,** 026501 (2013).

4. El Hadri, M. S. *et al.* Materials and devices for all-optical helicity-dependent switching. *Journal of Physics D: Applied Physics* **50,** 133002 (2017).

5. Kimel, A. V. & Li, M. Writing magnetic memory with ultrashort light pulses. *Nature Reviews Materials* **4,** 189–200 (2019).

6. Siddiqui, S. A. *et al.* Current-Induced Domain Wall Motion in a Compensated Ferrimagnet. *Physical Review Letters* **121,** 057701 (2018).

7. Caretta, L. *et al.* Fast current-driven domain walls and small skyrmions in a compensated ferrimagnet. *Nature Nanotechnology* **13,** 1154–1160 (2018).

8. Cai, K. *et al.* Ultrafast and energy-efficient spin–orbit torque switching in compensated ferrimagnets. *Nature Electronics* **3,** 37–42 (2020).

9. Yang, S. H. *et al.* Domain-wall velocities of up to 750 m s -1 driven by exchange-coupling torque in synthetic antiferromagnets. *Nature Nanotechnology* **10,** 221–226 (2015).

10. Lalieu, M. L. *et al.* Integrating all-optical switching with spintronics. *Nature Communications* **10,** 1–6 (2019).

11. Wang, L. *et al.* Picosecond Switching of Optomagnetic Tunnel Junctions. *arXiv* **2011.03612,** 1–18 (2020).

12. Koopmans, B. *et al.* Explaining the paradoxical diversity of ultrafast laser-induced demagnetization. *Nature Materials* **9,** 259–265 (2010).

13. Ostler, T. A. *et al.* Crystallographically amorphous ferrimagnetic alloys: Comparing a localized atomistic spin model with experiments. *Physical Review B* **84,** 024407 (2011).

14. Schellekens, A. J. & Koopmans, B. Microscopic model for ultrafast magnetization dynamics of multisublattice magnets. *Physical Review B* **87,** 020407 (2013).

15. Atxitia, U. *et al.* Controlling the polarity of the transient ferromagneticlike state in ferrimagnets. *Physical Review B* **89,** 224421 (2014).

16. Davies, C. *et al.* Pathways for Single-Shot All-Optical Switching of Magnetization in Ferrimagnets. *Physical Review Applied* **13,** 024064 (2020).

17. Beens, M. *et al.* Comparing all-optical switching in synthetic-ferrimagnetic multilayers and alloys. *Physical Review B* **100,** 220409 (2019).

18. Jakobs, F. *et al.* Unifying femtosecond and picosecond single-pulse magnetic switching in Gd-Fe-Co. *Physical Review B* **103,** 104422 (2021).

19. Haltz, E. *et al.* Domain wall dynamics in antiferromagnetically coupled double-lattice systems. *Physical Review B* **103,** 014444 (2021).

20. Buschow, K. H. J. Intermetallic compounds of rare-earth and 3d transition metals. *Reports on Progress in Physics* **40,** 1179–1256 (1977).

21. Radu, I. *et al.* Transient ferromagnetic-like state mediating ultrafast reversal of antiferromagnetically coupled spins. *Nature* **472,** 205–208 (2011).

22. Ostler, T. A. *et al.* Ultrafast heating as a sufficient stimulus for magnetization reversal in a ferrimagnet. *Nature Communications* **3,** 666 (2012).

23. Mentink, J. H. *et al.* Ultrafast Spin Dynamics in Multisublattice Magnets. *Physical Review Letters* **108,** 057202 (2012).

24. Graves, C. E. *et al.* Nanoscale spin reversal by non-local angular momentum transfer following ultrafast laser excitation in ferrimagnetic GdFeCo. *Nature Materials* **12,** 293–298 (2013).

25. Yang, Y. *et al.* Ultrafast magnetization reversal by picosecond electrical pulses. *Science Advances* **3,** 1–7 (2017).

26. Wilson, R. B. *et al.* Ultrafast magnetic switching of GdFeCo with electronic heat currents. *Physical Review B* **95,** 1–5 (2017).

27. Manchon, A. *et al.* Current-induced spin-orbit torques in ferromagnetic and antiferromagnetic systems. *Reviews of Modern Physics* **91,** 035004 (2019).

28. Finley, J. & Liu, L. Spin-Orbit-Torque Efficiency in Compensated Ferrimagnetic Cobalt-Terbium Alloys. *Physical Review Applied* **6,** 054001 (2016).

29. Mishra, R. *et al.* Anomalous Current-Induced Spin Torques in Ferrimagnets near Compensation. *Physical Review Letters* **118,** 167201 (2017).

30. Roschewsky, N. *et al.* Spin-orbit torque switching of ultralarge-thickness ferrimagnetic GdFeCo. *Physical Review B* **96,** 064406 (2017).

31. Je, S.-G. *et al.* Spin-orbit torque-induced switching in ferrimagnetic alloys: Experiments and modeling. *Applied Physics Letters* **112,** 062401 (2018).

32. Sala, G. *et al.* Real-time Hall-effect detection of current-induced magnetization dynamics in ferrimagnets. *Nature Communications* **12,** 656 (2021).

33. Gomonay, O. *et al.* High Antiferromagnetic Domain Wall Velocity Induced by Néel Spin-Orbit Torques. *Physical Review Letters* **117,** 017202 (2016).

34. Shiino, T. *et al.* Antiferromagnetic Domain Wall Motion Driven by Spin-Orbit Torques. *Physical Review Letters* **117,** 1–6 (2016).

35. Miron, I. M. *et al.* Perpendicular switching of a single ferromagnetic layer induced by in-plane current injection. *Nature* **476,** 189–193 (2011).

36. Baumgartner, M. *et al.* Spatially and time-resolved magnetization dynamics driven by spin-orbit torques. *Nature Nanotechnology* **12,** 980–986 (2017).

37. Martinez, E. *et al.* Universal chiral-triggered magnetization switching in confined nanodots. *Scientific Reports* **5,** 1–15 (2015).

38. Martínez, E. *et al.* Current-driven domain wall dynamics in ferrimagnets: Micromagnetic approach and collective coordinates model. *Journal of Magnetism and Magnetic Materials* **491,** 165545 (2019).

39. Bellouard, C. *et al.* Negative spin-valve effect in Co65Fe35/Ag/(Co65Fe35)50Gd50 trilayers. *Physical Review B* **53,** 5082–5085 (1996).

40. Tanaka, H. *et al.* Electronic-structure calculations for amorphous and crystalline Gd33Fe67 alloys. *Physical Review B* **46,** 7390–7394 (1992).

41. Zhou, W. *et al.* Spin-Hall and anisotropic magnetoresistance in ferrimagnetic Co-Gd/Pt layers. *Physical Review Materials* **2,** 1–7 (2018).

42. Lim, Y. *et al.* Dephasing of transverse spin current in ferrimagnetic alloys. *Physical Review B* **103,** 24443 (2021).

43. Bläsing, R. *et al.* Exchange coupling torque in ferrimagnetic Co/Gd bilayer maximized near angular momentum compensation temperature. *Nature Communications* **9,** 4984 (2018).

44. Chubykalo-Fesenko, O. *et al.* Dynamic approach for micromagnetics close to the Curie temperature. *Physical Review B* **74,** 094436 (2006).

45. Liu, T.-M. *et al.* Nanoscale Confinement of All-Optical Magnetic Switching in TbFeCo - Competition with Nanoscale Heterogeneity. *Nano Letters* **15,** 6862–6868 (2015).

46. Kirk, E. *et al.* Anisotropy-induced spin reorientation in chemically modulated amorphous ferrimagnetic films. *Physical Review Materials* **4,** 074403 (2020).

47. Beens, M. *et al.* The role of intermixing in all-optical switching of synthetic-ferrimagnetic multilayers. *AIP Advances* **9,** 125133 (2019).

48. Konar, B. *et al.* Critical Systematic Evaluation and Thermodynamic Optimization of the Fe-RE System: RE = Gd, Tb, Dy, Ho, Er, Tm, Lu, and Y. *Journal of Phase Equilibria and Diffusion* **38,** 509–542 (2017).

1   49.   Bernstein, P. & Gueugnon, C. Aging phenomena in TbFe thin films. *Journal of Applied*
2   *Physics* **55,** 1760–1762 (1984).

3   50.   Hansen, P. Chapter 4 Magnetic amorphous alloys. *Handbook of Magnetic Materials* **6,**
4   289–452 (1991).

1 Methods

2 Sample growth and device fabrication

The magnetic stacks were grown by magnetron sputtering on Si/SiN chips. The samples employed for transmission X-ray microscopy were deposited on SiN(200 nm) membranes transparent to the X-rays. The Ar pressure during the growth was 3 mTorr and the base pressure lower than 10^{-7} Torr. The deposited stacks were SiN/Ta(3)/Pt(5)/RE-TM/Ta(5)/Pt(1), where RE-TM stands for $Gd_xFe_yCo_{(1-x-y)}$(15), $Tb_xCo_{(1-x)}$(4), or a multilayer [Tb(0.25)/Co(0.25)]$_6$. The RE and TM elements of the GdFeCo and TbCo alloys were co-sputtered from elemental targets. The composition was varied by independently adjusting the power of the sputter guns and the deposition rates were calibrated by X-ray reflectivity. Blanket film samples and devices were grown at the same time. The device fabrication was performed by lift-off and subtraction techniques. The PMMA resist was spinned and baked at 180 °C for 10 minutes, exposed by e-beam lithography, and developed in a solution of MIBK and IPA. Then, thin films were deposited on the patterned resist and lifted off. The second step of e-beam lithography and the electron evaporation of Ti(25) defined the hard mask covering the dot (1-μm- and 500-nm-wide for GdFeCo and TbCo, respectively). In this second lithography step, the resist baking was skipped to avoid annealing the ferrimagnetic layers. Next, the Ti mask protected the device during the ion milling of the surrounding material, which was etched down to the Ta(3)/Pt(5) bilayer. The current line was contacted by Ti(5)/Au(50) pads fabricated by optical lithography and electron evaporation. Finally, 100 nm of Al were deposited on the back of the membranes to provide a heat sink during the measurements.

22 Scanning transmission X-ray microscopy

The X-ray measurements were performed at the PolLux beamline of the Swiss Light Source (Paul Scherrer Institut, Switzerland) and at the Maxymus beamline of the BESSY II electron storage ring (Helmholtz-Zentrum Berlin, Germany). A current-pump, X-ray-probe approach was employed to excite and detect the magnetization dynamics with both spatial and temporal resolution. The elemental sensitivity was provided by the X-ray magnetic circular dichroism (XMCD). Since this effect depends on the projection of the magnetization on the direction of the light polarization, the samples were oriented normally to the X-rays to probe the perpendicular component of the magnetization. The energy of the circularly-polarized X-rays with negative helicity was tuned to the L_3 and M_5 absorption edges of the transition-metal and rare-earth elements, respectively (Fe: 707 eV, Co: 778 eV, Gd: 1190 eV, Tb: 1243 eV). Monochromatic X-ray pulses with a 500 MHz repetition rate were focused onto the sample by a Fresnel zone plate and an order-selecting aperture. A typical image comprised about 35×35 pixels and was acquired by raster scanning the X-ray beam over an area of 1.2×1.2 μm^2, which corresponds to

1

a spatial resolution of 35 nm. The transmitted photons were collected by an avalanche photodiode whose output was routed to a field-programmable gate-array. The temporal resolution was determined by the duration of the X-ray pulses, in the order of 70 ps. The XMCD time traces were obtained by averaging the dichroic signal over the entire dot surface and then normalized to the steady-state signal.

The electric pulses were generated by an arbitrary waveform generator (Keysight M8195A, PolLux) or by a pulse-pattern generator (Keysight 81134A, Maxymus). The internal clock of these instruments was synchronized to the repetition rate of the light flashes (500 MHz, PolLux) or to the revolution frequency of the electron ring (1 MHz, Maxymus). The excitation pattern comprised sequences of set-reset pulses with similar amplitude and length and opposite polarity. The period of a set-reset unit was approximately 50 or 100 ns. The corresponding separation between the positive and negative pulses was usually set to 25 ns and 50 ns, respectively. The excitation was fed to a digital oscilloscope for monitoring purposes via a 20 dB pick-off-Tee. At each pixel, photons were collected typically for 500 ms, therefore each time trace was obtained by averaging the dynamics over $\sim 10^{10}$ pulse sequences.

The device under test was wire bonded to a printed circuit board, and its status was continually checked by monitoring its DC resistance. A 50 Ohm resistor was connected in parallel to ensure the impedance matching. The in-plane magnetic field was controlled by an electro-mechanical magnet. O_2 (PolLux) or He (Maxymus) at the pressure of 5-10 mbar was injected in the chamber prior to the measurements to improve the cooling of the devices and, in the case of O_2, limit the carbon deposition over the scanned area.

Micromagnetic simulations

The micromagnetic simulations have been performed with a custom-made, mumax3-based code [1] that takes into account the individual sublattices (S1: Fe, S2: Gd) forming the ferrimagnetic dot (thickness: 15 nm; diameter: 512 nm). It solves the coupled Landau-Lifschitz-Gilbert (LLG) equations of the two sublattices, linked by the antiferromagnetic coupling. The code includes the spin-orbit torques (SOT) and the spin transfer torques (STT). The LLG equation of the $i^{th} = 1, 2$ sublattice reads:

$$\frac{d\boldsymbol{m}_i}{dt} = -\gamma_i \boldsymbol{m}_i \times \boldsymbol{H}_i^{eff} + \alpha_i \boldsymbol{m}_i \times \frac{d\boldsymbol{m}_i}{dt} + \boldsymbol{\tau}_i^{SOT} + \boldsymbol{\tau}_i^{STT} \tag{1}$$

where $\boldsymbol{m}_i(\boldsymbol{r}, t) = \boldsymbol{M}_i(\boldsymbol{r}, t)/M_{s,i}$ is the normalized local magnetization. $\boldsymbol{H}_i^{eff}$ is the total effective magnetic field, which includes the external magnetic field, the effective anisotropy, the Dzyaloshinskii-Moriya interaction (DMI), and the intra-lattice and inter-lattice exchange interactions. The latter is modelled by the antiferromagnetic exchange field $\boldsymbol{H}_{AF,i}$ given by $\boldsymbol{H}_{AF,i} = -\frac{1}{\mu_0 M_{s,i}} \frac{\delta E_{ex}}{\delta \boldsymbol{m}_i}$. Here, $E_{ex} = -C_{ex} \boldsymbol{m}_i \cdot \boldsymbol{m}_j$ is the energy density of the antiferromagnetic coupling, whose strength is determined by the parameter C_{ex}. In the present study, the latter was

2

varied to reproduce the different experimental observations. Estimations of the values of C_{ex} can be found in Supplementary Note 7. α_i and $\gamma_i = \mu_0 g_i \mu_B / \hbar$ are the Gilbert damping and the gyromagnetic ratio of each sublattice, respectively, with g_i the Landé factor. μ_0, μ_B, and $\hbar$ are the permittivity of free space, the Bohr magneton, and the reduced Planck's constant, respectively. $\boldsymbol{\tau}_i^{SOT}$ and $\boldsymbol{\tau}_i^{STT}$ are the SOT and STT contributions. The details of the micromagnetic code can be found in Ref. [2].

The material parameters used for the simulations presented in the main text are summarized in Table T1. The intra-lattice exchange constant $A_{ex,i}$ was in the order of 10 pJ/m for both sublattices [3, 4]. Typical Landé factors g were taken from the literature [5–7]. The net spontaneous magnetization M_s of each sublattice was estimated from SQUID measurements on blanket films grown together with the devices (see Supplementary Note 1). The effective anisotropy constant K_{eff} was assumed to be in the order of a few kJ/m^3 because of the small single-ion anisotropy of Gd. These values match with the anisotropy energy extracted from the magnetic hysteresis loop of the devices and are in agreement with previous reports [8, 9]. We took a DMI energy density of ≤ 0.2 mJ/m^2, which is one order of magnitude smaller than in ultra-thin ferromagnetic films on top of a Pt layer and similar to other ferrimagnetic systems [10, 11]. The strength of the damping-like SOT was described by an effective spin Hall angle $\theta_{SH,i} \approx 0.20$ [12–14] that is larger for the transition-metal sublattice because of its preponderant contribution to magneto-transport effects. The influence of the field-like SOT and STT was found to be minimal when using the field-like parameter $\varepsilon_{1,2} = \pm 0.02$, the STT polarizations $P_1 = 0.15$ and $P_2 = 0.35$, the non-adiabatic parameter $\beta_{1,2} = 0.1$, and a current density in the GdFeCo layer $J_{STT} = 0.5$ TA/m^2 [1].

Temperature effects have been taken into account by modelling the temperature with the equations $T(t) = T_0 + \Delta T (1 - e^{-t/\tau})$ and $T(t) = T_f + \Delta T e^{-t/\tau}$, respectively for the increase of the temperature during the pulse and its decay afterwards [15, 16]. We considered the following conditions: $T_0 = 300$ K; $\Delta T = 30\text{-}70$ K, $\tau = 0.2\text{-}7$ ns. Simulations performed with temperature-dependent magnetization, anisotropy, and DMI confirmed that the results valid at constant temperature still hold in the presence of temperature variations caused by Joule heating.

An in-plane magnetic field $\mu_0 H_x = 20$ mT was oriented along the current direction, and current pulses with alternate polarity were applied. In order to mimic realistic conditions, we simulated the effects of a grainy magnetic texture with a characteristic size of 10 nm. Within each grain, the easy-axis perpendicular anisotropy had a small random in-plane component [17, 18] corresponding to a maximum deviation of the magnetization from the out-of-plane direction of 10%. Finally, thermal fluctuations were included by means of a random thermal field. The results remain valid even in the absence of grains and thermal fluctuations.

Scanning-transmission electron microscopy and energy-dispersive X-ray spectroscopy

Parameter, S1/S2	Value
Inter-lattice exchange coupling, C_{ex} [kJ/m^3]	-6.8
Intra-lattice exchange stiffness, A_{11}/A_{22} [pJ/m]	16/11
Saturation magnetization, $M_{s,1}/M_{s,2}$ [MA/m]	0.26/0.30
Anisotropy energy density, $K_{eff,1}/K_{eff,2}$ [kJ/m^3]	8.7/8.7
DMI energy, D_1/D_2 [mJ/m^2]	0.09/09
Gilbert damping, α_1/α_2	0.05/0.05
Landé factor, g_1/g_2	2.20/1.95
Effective spin Hall angle, $\theta_{SH,1}/\theta_{SH,2}$	0.21/0.07
Longitudinal magnetic field, $\mu_0 H_x$ [mT]	20
Electric-current density, J [TA/m^2]	2
Electric-pulse duration, t_p [ns]	1.5

Table T1. Simulation parameters. The subscripts 1 and 2 refer to the FeCo and Gd sublattices, respectively.

Scanning transmission electron microscopy (STEM) and energy-dispersive X-ray spectroscopy (EDX) measurements were performed on a FEI Titan Themis equipped with a probe CEOS DCOR spherical aberration corrector and ChemiSTEM technology operated at 300 kV. A probe convergence semiangle of 18 mrad was used in combination with a collection angular range for the high-angle annular dark field (HAADF) detector set to 66-200 mrad.

Thin lamellas of the samples were cut in cross-section by means of a FEI Helios Nanolab 600i focused ion beam (FIB) instrument at accelerating voltages of 30 and 5 kV after deposition of C and Pt protective layers. Two samples with nominally identical $Gd_{31}Fe_{62}Co_7$ composition were compared. The first sample (aged), grown simultaneously with the device whose measurements are presented in Fig. 2a,b, was 30 months old at the time of the STEM measurements. The second sample (fresh) was grown 4 weeks before the characterization with the same recipe as the first one. We estimated by Rutherford backscattering spectroscopy that the Gd concentration was the same in the two samples within an uncertainty of less than 2%.

The composition of the samples was evaluated by EDX mapping and the elemental maps of the C-K, N-K, O-K, Si-K, Fe-K, Co-K, Ta-L, Pt-L and Gd-L signals were extracted from the spectrum image. The elemental profiles of Fe and Gd across the $Gd_{31}Fe_{62}Co_7$ layer thickness were calculated by averaging over the horizontal direction in Fig. 5a,d. The correlation image was obtained by calculating at each pixel i the quantity $\frac{f_i - F}{s_f} \frac{g_i - G}{s_g}$, where f_i (g_i) is the ith pixel intensity in the map of Fe (Gd), F (G) is the corresponding average image intensity, and s_f (s_g) the standard deviation [19]. The correlation coefficient was then calculated as $\frac{1}{N-1} \sum_i^N \left(\frac{f_i - F}{s_f} \right) \left(\frac{g_i - G}{s_g} \right)$,

4

where N is the number of pixels. As an alternative to this method, the correlation coefficient was also determined by comparing the intensity of the Fe and Gd STEM-EDX images, averaged along the vertical direction, as described in detail in Supplementary Note 12. Both approaches yield a higher anticorrelation in the fresh sample relative to the aged sample.

References

1. Vansteenkiste, A. *et al.* The design and verification of MuMax3. *AIP Advances* **4,** 107133 (2014).

2. Martínez, E. *et al.* Current-driven domain wall dynamics in ferrimagnets: Micromagnetic approach and collective coordinates model. *Journal of Magnetism and Magnetic Materials* **491,** 165545 (2019).

3. Vittoria, C. *et al.* Magnetic properties of amorphous and crystalline GdFe2. *Journal of Applied Physics* **49,** 4908–4917 (1978).

4. Xian-Ying, W. *et al.* Temperature-Induced Magnetization Reorientation in GdFeCo/TbFeCo Exchange-Coupled Double Layer Films. *Chinese Physics Letters* **20,** 1359–1361 (2003).

5. Kittel, C. On the Gyromagnetic Ratio and Spectroscopic Splitting Factor of Ferromagnetic Substances. *Physical Review* **76,** 743–748 (1949).

6. Scott, G. G. Review of Gyromagnetic Ratio Experiments. *Reviews of Modern Physics* **34,** 102–109 (1962).

7. Okuno, T. *et al.* Temperature dependence of magnetic resonance in ferrimagnetic GdFeCo alloys. *Applied Physics Express* **12,** 093001 (2019).

8. Hansen, P. *et al.* Magnetic and magneto-optical properties of rare-earth transition-metal alloys containing Gd, Tb, Fe, Co. *Journal of Applied Physics* **66,** 756–767 (1989).

9. Dai, B. *et al.* Spin Transfer Torque Switching of Amorphous GdFeCo With Perpendicular Magnetic Anisotropy for Thermally Assisted Magnetic Memories. *IEEE Transactions on Magnetics* **48,** 3223–3226 (2012).

10. Finley, J. & Liu, L. Spin-Orbit-Torque Efficiency in Compensated Ferrimagnetic Cobalt-Terbium Alloys. *Physical Review Applied* **6,** 054001 (2016).

11. Bläsing, R. *et al.* Exchange coupling torque in ferrimagnetic Co/Gd bilayer maximized near angular momentum compensation temperature. *Nature Communications* **9,** 4984 (2018).

12. Yang, Y. *et al.* Ultrafast magnetization reversal by picosecond electrical pulses. *Science Advances* **3,** 1–7 (2017).

13. Roschewsky, N. *et al.* Spin-orbit torques in ferrimagnetic GdFeCo alloys. *Applied Physics Letters* **109,** 112403 (2016).

14. Je, S.-G. *et al.* Spin-orbit torque-induced switching in ferrimagnetic alloys: Experiments and modeling. *Applied Physics Letters* **112,** 062401 (2018).

15. Moretti, S. *et al.* Influence of Joule heating on current-induced domain wall depinning. *Journal of Applied Physics* **119,** 213902 (2016).

16. Raposo, V. *et al.* Domain wall dynamics along curved strips under current pulses: The influence of Joule heating. *Applied Physics Letters* **108,** 042405 (2016).

17. Torrejon, J. *et al.* Tunable inertia of chiral magnetic domain walls. *Nature Communications* **7,** 1–7 (2016).

18. P. del Real, R. *et al.* Current-Induced Generation and Synchronous Motion of Highly Packed Coupled Chiral Domain Walls. *Nano Letters* **17,** 1814–1818 (2017).

19. Johnson, G. R. *et al.* Investigations of element spatial correlation in Mn-promoted Co-based Fischer-Tropsch synthesis catalysts. *Journal of Catalysis* **328,** 111–122 (2015).

Author contributions

P.G., G.S., and C.H.L. planned the experiment. G.S., C.H.L., V.K., and G.K. performed the STXM measurements with the support of S.F., M.W., and J.R.. G.S. characterized the magnetic properties of full films and devices. E.M. and V.R. developed the micromagnetic code and performed the simulations. M.R. performed the STEM characterization. M.R and G.S. analyzed the STEM-EDX maps. G.S. and P.G. analyzed the data and wrote the manuscript with inputs from E.M.. All authors discussed the data and commented on the manuscript.

Competing interests

The authors declare no competing interests.